Comparative analysis of nonlinear optofluidic processes in microdroplets

Peng Zhang and Sunghwan Jung*
Department of Biomedical Engineering and Mechanics, Virginia Tech, Blacksburg, Virginia 24061, USA

Aram Lee and Yong Xu†
Department of Electrical and Computer Engineering, Virginia Tech, Blacksburg, Virginia 24061, USA
(Received 13 April 2016; published 29 June 2016)

Our prior work has shown that high quality (Q) factor whispering gallery modes (WGMs) in liquid microdroplets can potentially induce single-photon-level nonlinear effects through radiation pressure on the interface. However, little is known about the nonlinear effects of other processes involving scattering force and thermocapillarity. In this study, we establish a numerical framework that can calculate the fluid motion and the resultant nonlinearity induced by the optical scattering force and thermocapillarity. Then, we compare the magnitude of various nonlinear optofluidic processes induced by the radiation pressure, the thermocapillary effect, the scattering-induced optical force, and the Kerr effect. Using realistic fluid parameters, we show that the radiation pressure due to the WGM produces the strongest nonlinear optofluidic effect.

DOI: 10.1103/PhysRevE.93.063119

I. INTRODUCTION

Optofluidics was originally developed for important applications such as lasing [1], sensing [2,3], and display [4–6]. The mechanical interplay between light and liquid, however, has not been thoroughly investigated, even though the first demonstration of liquid motion actuated by a focused laser beam was reported as early as 1973 [7]. Since the classic work by Ashkin and Dziedzic, the distortion of a liquid system induced by a high intensity laser beam has been studied in [4,8–16], where both flat and spherical fluid interfaces were considered.

Recently, in Ref. [17,18], we analyzed a highly nonlinear optofluidic system that is composed of light circulating in a liquid droplet in the form of a high quality (Q) factor whispering gallery mode (WGM). In such a system, the radiation pressure of the high-Q WGM can push the droplet surface outward and form the bulge depicted in Fig. 1. Perhaps the most interesting result of our theoretical analysis is that the strength of the radiation pressure induced nonlinearity exceeds that of the Kerr nonlinearity by up to six orders of magnitude. As a result, the radiation pressure induced nonlinear optofluidics may ultimately produce nonlinear effects at single-photon energy level. Our prior work only considered nonlinear effects due to the radiation pressure. Yet besides radiation pressure, optical fields can also actuate fluid motions through scattering force [13] and thermocapillary force [19]. In this paper, we compare the magnitude of nonlinear effects induced by the scattering force and the thermocapillary force, as well as radiation pressure induced nonlinearity and other nonlinear effects.

When light is elastically scattered by inhomogeneities in a fluid (e.g., suspended particles or density fluctuations), the light momentum can be changed, which results in a scattering force that may induce fluid motion in the volume. For example, a cylindrical dripping liquid jet was produced by light scattering in a microemulsion and the dripping rate was theoretically predicted [20]. The fluid motion due to the light scattering was also observed in a fluid layer with a flat interface [21], where a toroidal fluid recirculation was produced by a vertically incident laser beam. The scattering force induced an interface deformation that was found to be of the same order of magnitude as the deformation induced by the radiation pressure. The effects of light scattering in a similar setup were simulated numerically by the boundary element method in [14], which showed good agreement with experimental observations. In these studies, the scattering force in the fluid has been modeled as a body force that depends on the light intensity. Similarly, in the case of WGMs circulating in a liquid droplet, the effect of light scattering should also produce a body force in liquid resonators in the same direction as the WGM propagation. For experimental studies of nonlinear effects in microdroplets, it is highly relevant to theoretically estimate the magnitude of interfacial deformation due to the scattering force.

Another potentially relevant factor is the thermocapillary force. The localized light heating in the liquid may result in a temperature gradient, which leads to thermocapillary stresses on the fluid interface. The thermocapillary effect of laser heating has been applied in drop sorting, merging and microfluidic valves [19,22,23], etc. Baroud *et al.* [19] demonstrated that the thermocapillary force could induce a circulation of fluid in a droplet and thus control the motion of the droplet. In our work on microdroplets as whispering gallery resonators [18], we computed the temperature increase due to the WGM energy absorption, from which the volume expansion and refractive index change were estimated. Since the temperature varies along the fluid interface, the thermocapillary effect may arise and induce interfacial flow on the droplets. Such effect can therefore lead to another class of nonlinear optofluidic processes, which was not analyzed quantitatively in our previous publication [18].

The objective of this work is to develop a boundary element model to evaluate the nonlinear optofluidic effects induced by the light scattering and the thermocapillary force associated with the WGMs in microdroplets. We quantify the magnitudes of these two nonlinear processes, and compare them with

*sunnyjsh@vt.edu
†yong@vt.edu

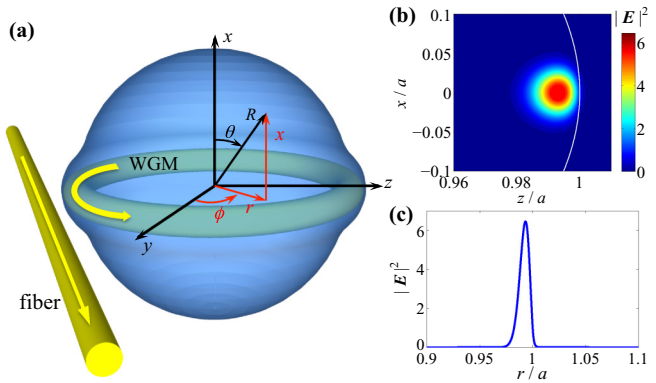

FIG. 1. (a) Schematics of a high-Q WGM circulating along the equator of a droplet induced by the laser propagating in a nearby fiber. The yellow arrows indicate light propagation directions. A cylindrical coordinate (x,r,ϕ) and a spherical coordinate (R,θ,ϕ) are defined to assist further analysis. (b) The electric field intensity $|\boldsymbol{E}|^2$ of the WGM in a $a = 100$ μm droplet within the x-z plane. The white curve indicates the droplet interface. (c) The $|\boldsymbol{E}|^2$ distribution along the radial direction within the $x = 0$ plane. The $|\boldsymbol{E}|^2$ field shown in (b) and (c) has been normalized by its maximum value on the interface.

nonlinearities induced by the radiation pressure as well as the thermal and Kerr effects. Specifically, in Sec. II, the boundary element formulations for Stokes equations with scattering force and thermocapillary force are derived in an axisymmetric domain. The fluid motion induced by various optofluidic processes are analyzed and compared in Sec. III. The nonlinearities associated with the interfacial deformation are also compared with purely thermal effects such as volume expansion and refractive index changes induced by temperature changes, as well as the Kerr nonlinearity.

II. OPTICAL FIELD INDUCED FLUID MOTION

We consider a system of a high-index liquid microdroplet (core) immersed in a low-index immiscible fluid (cladding). Such a system can support a high-Q WGM circulating along the equator of the droplet, as illustrated in Fig. 1. By assuming a transverse electric (TE) mode, the optical field in the resonator has been calculated analytically in [17,24], the derivations of which will not be repeated here. In this paper, we denote variables associated with the core phase with subscript "co" and the cladding phase with subscript "cl".

In this section, we derive boundary element models to quantitatively calculate the fluid motion actuated by the scattering force, thermocapillary force, and radiation pressure induced by the WGM in the droplet.

A. Effect of light scattering

Due to the fluid inhomogeneity, the optical field in the droplet can induce a scattering force in the same direction as the light propagation [14,20],

$$\boldsymbol{F} = \varpi \frac{n_{co}}{c} S_\phi \boldsymbol{e}_\phi, \tag{1}$$

where ϖ is the forward light momentum attenuation coefficient (or turbidity), n_{co} is the refractive index of the core phase, c is the speed of light, and S_ϕ is the ϕ component of the Poynting vector, which represents the light intensity. Note that S_ϕ (and thus $\boldsymbol{F}$) is independent of ϕ. Due to its direction, the scattering force $\boldsymbol{F}$ may cause a circulational motion of the fluid. With known force magnitude, it is possible to compute the fluid velocity numerically.

The motions of the fluid interface and volume are governed by the Navier-Stokes equations. For a typical drop with radius $a \sim 100$ μm, characteristic velocity $U \sim 10^{-3}$ m/s, density difference $\rho \sim 200$ kg/m^3, and fluid viscosity $\mu \sim 13$ mPa s, the Reynolds number is approximately $\mathrm{Re} = \rho U a/\mu \sim 10^{-2}$. As a consequence of the low Reynolds number, the Stokes assumption is valid for our system. In the presence of the scattering force, the Stokes equations and incompressibility condition can be written as

$$-\nabla p_d + \mu \nabla^2 \boldsymbol{u} + \boldsymbol{F} = 0, \quad \nabla \cdot \boldsymbol{u} = 0, \tag{2}$$

where the dynamic pressure p_d is defined as the sum of actual fluid pressure and centrifugal effect of the fluid motion $p_d = p + \rho u_\phi^2/2$.

The boundary element method (BEM) has been widely used to solve the stokes equations numerically [25–27]. For a two-phase fluid system with a sharp interface in the three-dimensional domain, the interfacial velocity and pressure are related by the following boundary integral equations (BIE):

$$\begin{aligned} u_j(\boldsymbol{x}_0) = {} & b_1 \int_S G_{ji}(\boldsymbol{x}_0,\boldsymbol{x}) f_i(\boldsymbol{x})\, dS(\boldsymbol{x}) \\ & + b_2 \int_S u_i(\boldsymbol{x}) K_{ijm}(\boldsymbol{x}_0,\boldsymbol{x}) n_m(\boldsymbol{x})\, dS(\boldsymbol{x}) \\ & + b_1 \int_V G_{ji}(\boldsymbol{x}_0,\boldsymbol{x}) F_i(\boldsymbol{x})\, dV(\boldsymbol{x}), \end{aligned} \tag{3}$$

where $b_1 = -1/[4\pi\mu_{cl}(1+\lambda)]$; $b_2 = (1-\lambda)/[4\pi(1+\lambda)]$; $\lambda = \mu_{co}/\mu_{cl}$ is the viscosity ratio of the core and cladding phases; $\boldsymbol{f}$ is the total stress on the interface; S denotes the interface of the droplet; position vectors $\boldsymbol{x}$ and $\boldsymbol{x}_0$ are located on the fluid interface. Indices i,j,m take values of 1,2,3 and repeated indices are summed. The Green's functions G_{ij} and K_{ijm} for Stokes flow in free space take the form

$$G_{ij}(\boldsymbol{x},\boldsymbol{y}) = \frac{1}{s}\delta_{ij} + \frac{1}{s^3} s_i s_j, \quad K_{ijm}(\boldsymbol{x},\boldsymbol{y}) = -\frac{6}{s^5} s_i s_j s_m, \tag{4}$$

with $s_i = x_i - y_i$, $s = |\boldsymbol{s}|$, and δ_{ij} is the identity tensor.

Due to the axial symmetry of the droplet geometry, boundary conditions, as well as the WGM-induced scattering force, all the velocity and force variables in Eq. (3) should be independent of the coordinate ϕ. Therefore, we can integrate Eq. (3) over the ϕ direction analytically to lower the dimension of numerical discretization and integration. We can show that the integration over ϕ direction results in the decomposition of Eq. (3) into the following x-r and ϕ components:

$$\begin{aligned} u_\alpha(\boldsymbol{x}_0) = {} & b_1 \int_C M_{\alpha\beta}(\boldsymbol{x}_0,\boldsymbol{x}) f_\beta(\boldsymbol{x}) dl(\boldsymbol{x}) \\ & + b_2 \int_C Q_{\alpha\beta\gamma}(\boldsymbol{x}_0,\boldsymbol{x}) u_\beta(\boldsymbol{x}) n_\gamma(\boldsymbol{x}) dl(\boldsymbol{x}), \end{aligned} \tag{5a}$$

$$\begin{aligned} u_\phi(\boldsymbol{x}_0) = {} & b_2 \int_C u_\phi(\boldsymbol{x}) Q_{\phi\phi\gamma}(\boldsymbol{x}_0,\boldsymbol{x}) n_\gamma(\boldsymbol{x}) dl(\boldsymbol{x}) \\ & + b_1 \int_A F_\phi(\boldsymbol{x}) M_{\phi\phi}(\boldsymbol{x}_0,\boldsymbol{x}) dA(\boldsymbol{x}). \end{aligned} \tag{5b}$$

In Eq. (5), indices α,β,γ take the value of 1 and 2, representing the x and r directions, respectively. C and A represent the interface and the volume of the fluid domain intercepted with a $\phi =$ constant plane. Note that Eq. (5a) is the same as the BIE in axisymmetric domain with no ϕ component of velocity or force derived in literature [26], whereas Eq. (5b) is the new BIE that governs the swirling motion of the fluid induced by the azimuthal component of the scattering force. As shown by Eq. (5), the ϕ component of the velocity field is decoupled from u_x and u_r. However, the centrifugal effect of u_ϕ can produce an interface force that subsequently induces fluid motion in x and r directions. This is evidenced by the expression of the total force on the interface,

$$\boldsymbol{f} = \left(2\sigma\kappa_m - \Delta\rho u_\phi^2/2\right)\boldsymbol{n}, \tag{6}$$

where κ_m is the mean curvature of the interface. The detailed derivations of Eq. (5) are shown in Appendix A.

In our simulations, the fluid interface on the $\phi =$ constant plane is discretized into N circular arc elements, and $\boldsymbol{x}_0$ is located at the center of each element. On each element, the surface velocity and pressure are assumed to be constant, and the axisymmetric Green's functions are integrated numerically using Gauss quadrature. Note that Green's functions may exhibit logarithmic singularities as $\boldsymbol{x} \to \boldsymbol{x}_0$, and special treatment is needed to ensure the accuracy of numerical integration. The detailed derivations of the singularity behaviors and their numerical integration schemes are shown in Appendix B.

Equation (5) can then be discretized and written as linear systems relating the unknown interface velocity vector $(\{v^{xr}\},\{v^\phi\})$ with the interface force vector $(\{f\})$ or the volume force integral $(\{I^F\})$:

$$[A]\{v^{xr}\} = [B]\{f\}, \tag{7a}$$

$$[H]\{v^\phi\} = \left\{I^F\right\}, \tag{7b}$$

where $[A]$, $[B]$, and $[H]$ are matrices whose entries are related to the integrals of $M_{\alpha\beta}$ and $Q_{\alpha\beta\gamma}n_\gamma$ on the interface elements.

In the simulation, the linear system Eq. (7b) is solved first and the u_ϕ distribution is obtained. The total interface force including the centrifugal effect of u_ϕ is then computed and used in Eq. (7a), the solution to which results in the velocity components within the $\phi =$ constant plane. The solution to the above linear systems gives the velocity at the center of each element on the interface. Velocity values at the end points of each element are interpolated by a cubic spline with vanishing derivatives at $x = \pm a$. The element edges and center displacements are integrated over a time step Δt by the explicit Euler scheme, i.e., $\Delta\boldsymbol{x} = \boldsymbol{u}\Delta t$, and a new interface shape is produced for the following time step. At each time step, a new linear system Eq. (7) is generated based on the updated interface shape. The time step size is chosen by the criterion $\Delta t \leqslant \tau_m = (\mu_{co} + \mu_{cl})\delta/(2\sigma)$, where δ is the element size [28]. This process is iterated until the maximum velocity magnitude $|\boldsymbol{u}|$ is 1000 times smaller than the initial velocity magnitude. In our simulations, we find that $N = 128$ elements can provide results with adequate accuracy.

B. Thermocapillary effect

As shown in [18], the absorption of the WGM energy by the droplet may result in the temperature change in the fluid, which should increase the droplet volume and change its refractive index. In addition, the temperature gradient on the fluid interface can also induce the thermocapillary effect, i.e., a shear stress along the interface. Using the well-known Eötvös rule [29], the interfacial tension of the fluid system at a given temperature T is

$$\sigma = \bar{k}\bar{V}^{-2/3}(T_c - T), \tag{8}$$

where $\bar{k}$ and $\bar{V}$ are material properties and T_c is the critical temperature of the fluid. Assuming that the interfacial tension at room temperature T_0 is σ_0, the value of σ can then be derived as

$$\sigma = \sigma_0\frac{T_c - T}{T_c - T_0}. \tag{9}$$

With known temperature distribution on the fluid interface, the gradient of the interfacial tension, $\partial\sigma/\partial s$, can be calculated and the total stress on the interface is

$$\boldsymbol{f} = (2\sigma\kappa_m)\boldsymbol{n} - (\partial\sigma/\partial s)\boldsymbol{t}. \tag{10}$$

The fluid velocity induced by the thermocapillary effect can then be computed by Eqs. (5a) and (7a).

Note that as modeled in Ref. [18], the fluid motion induced by the optical radiation pressure, $p_{\text{opt}} = \frac{1}{2}\epsilon_0(n_{co}^2 - n_{cl}^2)|\boldsymbol{E}_{\text{surf}}|^2$ [9,17], is also governed by Eqs. (5a) and (7a) with the total stress on the interface $\boldsymbol{f} = (2\sigma\kappa_m - p_{\text{opt}})\boldsymbol{n}$.

So far, we have developed BEM models that can simulate the fluid motion and interface dynamics of the droplets under scattering force, thermocapillary and radiation pressure effects. In the following section, the fluid motion and the interface deformation induced by the aforementioned nonlinear optofluidic processes will be computed and their magnitudes will be compared.

III. WGM INDUCED NONLINEAR PROCESSES IN LIQUID DROPLETS

In this study, we choose a liquid system based on an oil droplet immersed in water, which has the same properties as the system analyzed in [18]. Fluid viscosities of the core and cladding media are $\mu_{co} = 13$ mPa s and $\mu_{cl} = 1$ mPa s. The forward light momentum attenuation coefficient of the core fluid is assumed to be $\varpi = 70\ \text{m}^{-1}$. (For a transparent liquid with low attenuation, such as an index matching fluid, the value of $\varpi = 70\ \text{m}^{-1}$ is likely an overestimate. However, as will be shown later, a more accurate estimate for ϖ is unnecessary.) The oil-water interfacial tension at room temperature is $\sigma = 30$ mN/m. The properties of the WGMs depend on the liquid refractive indices as well as the geometry of the resonator. This liquid droplet can possess high Q factor in the visible wavelength range. For simplicity, we choose the WGM wavelength to be $\lambda \approx 700$ nm, with the effective refractive indices of the core and cladding phases $n_{co} = 1.44$ and $n_{cl} = 1.33$, respectively. The mode numbers and resonance wavelengths of the fundamental WGMs $|l,l\rangle$ are provided by [18] and shown in Table I. The electric field $\boldsymbol{E}$ and the Poynting vector ϕ-component (S_ϕ) distribution

TABLE I. Angular mode number l and resonance wavelength λ of WGMs in liquid droplets [18].

a (μm)	400	300	250	200	150	120
l	5145	3847	3204	2569	1918	1529
λ (nm)	699.35	700.66	700.45	698.05	699.95	701.26
a (μm)	100	80	70	60	50	40
l	1275	1018	889	761	632	504
λ (nm)	699.75	699.65	700.05	699.75	700.55	700.59

are computed following the formula provided in Ref. [18]. The circulating WGM power is assumed to be 1 W for all calculations in this work.

In this section, the fluid motion in the droplet as a result of the radiation pressure, light scattering and thermocapillarity are calculated following the numerical procedure described in Sec. II. The optofluidic nonlinearities due to the interface deformation are computed and compared.

A. WGM induced fluid motion

We first look at the fluid motion due to the light scattering force, Eq. (1), in the volume of the droplet. The rotational velocity (u_ϕ) of the droplet is shown in Fig. 2. The rotational motion of the droplet leads to an centrifugal force on the interface, which results in a velocity field on the x-r plane. This velocity field at $t = 0$ is shown in Fig. 4(a).

The fluid motion induced by the radiation pressure has been studied in [18], which is also shown in Fig. 4(b). To calculate the thermocapillary effect, the temperature distribution on the droplet interface is also computed by the BEM. The detailed BEM formulations are available in [18] and the steady state temperature increase on the droplet interface is shown in Fig. 3. With the shear stress due to the interfacial tension gradient given by Eqs. (9) and (10), the fluid motion in the droplet can be produced by the BIE (5a), which is shown in Fig. 4(c). As evidenced in Fig. 4, the velocity field in the x-r plane due to the droplet rotation is several orders of magnitude smaller than the velocity induced by the radiation pressure and thermocapillarity.

The droplet interface deforms under nonzero u_x and u_r distribution on the interface. The interface forces under the

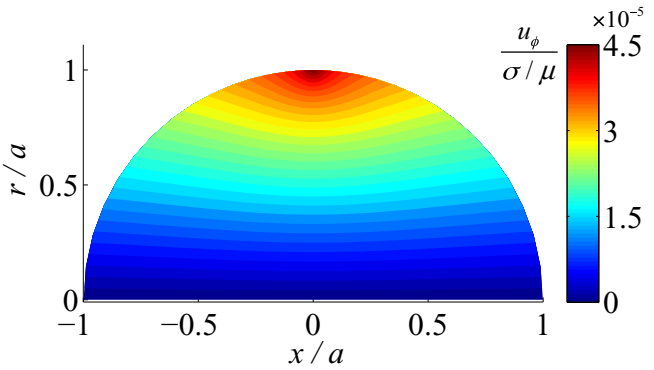

FIG. 2. Velocity u_ϕ component distribution induced by light scattering in the volume of the $a = 100$ μm droplet on a ϕ = constant plane.

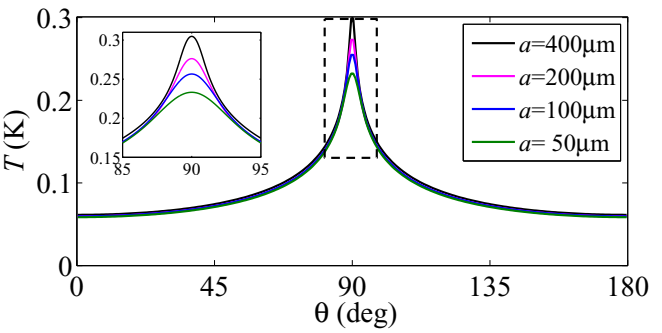

FIG. 3. Variation of the steady state temperature increase on interfaces of droplets with radii $a = 50,100,200,400$ μm as a result of thermal heating. A zoomed view of the boxed region is shown in the inset.

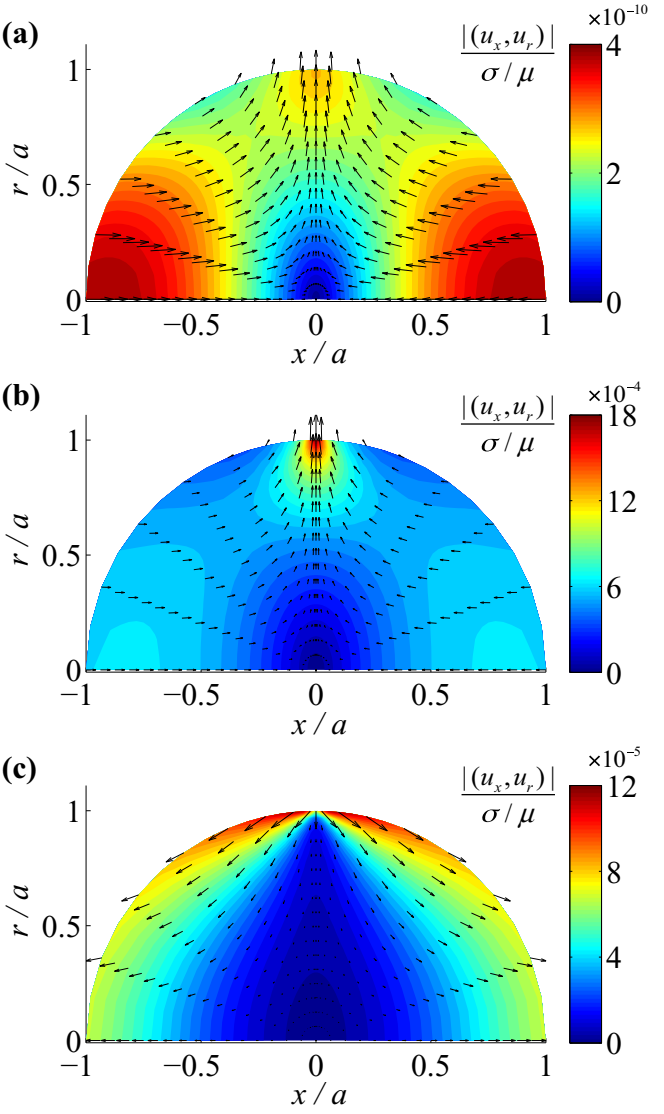

FIG. 4. Velocity distribution in the x,r directions at $t = 0$ induced by (a) light scattering in the fluid, (b) radiation pressure, and (c) thermocapillary effect on the interface of the $a = 100$ μm droplet on a ϕ = constant plane.

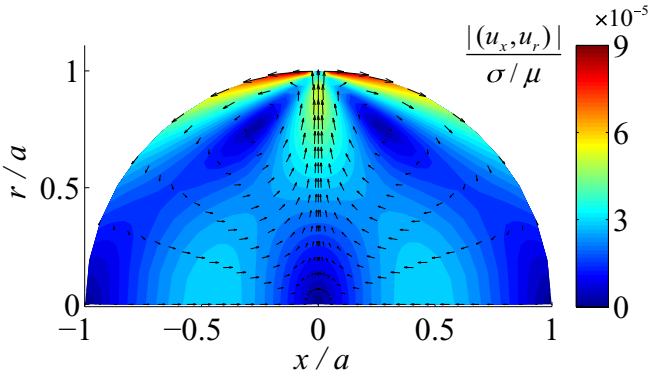

FIG. 5. Velocity distribution as a result of the thermocapillary effect in a droplet with balanced interface shape. The radius of the droplet is $a = 100\ \mu$m.

effect of centrifugal force and radiation pressure are eventually balanced by the surface tension force resulting from the interface deformation. On the other hand, the shear stress due to thermocapillarity would still actuate fluid motion on a balanced droplet. The velocity field in a balanced droplet due to thermocapillarity is shown in Fig. 5. Similar to the fluid motion reported in other systems [19], Fig. 5 shows that fluid circulations are also present in our system.

Under the velocity field shown in Fig. 4, the balanced interface shape can be obtained by time integration of the interface position until the normal component of the interface velocity vanishes. The droplet interface deformation for all the twelve cases shown in Table I under the effects of radiation pressure, light scattering, and thermocapillarity are shown in Fig. 6. Since the overall shapes of the interface deformation are self-similar, when normalized by the interface displacement at $\theta = \pi/2$, each curve shown in Fig. 6 is in fact a collection

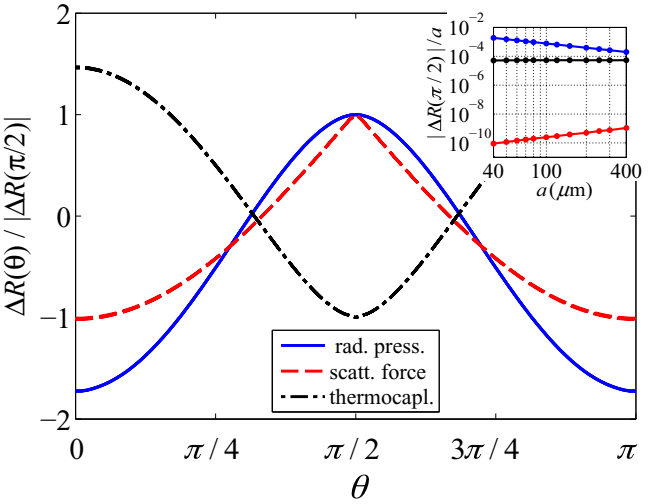

FIG. 6. Droplet interface deformation under the effects of radiation pressure, light scattering, and thermocapillarity, normalized by the interface displacement magnitude at $\theta = \pi/2$. Due to the normalization, each curve shown here is in fact a collection of twelve curves (see Table I) collapsed together. The inset shows the magnitude of the droplet interface deformation at the equator ($|\Delta R(\pi/2)/a|$).

of results for the twelve microdroplets listed in Table I, each with a different radius. We also observe that the interface deformation induced by the light scattering is several orders of magnitude smaller than the radiation pressure effect. This phenomenon is different from the results reported on a flat fluid interface [14], where micron-scale deformation was induced by the scattering of a vertically incident laser beam. On a flat fluid interface, the scattering force and the radiation pressure were in parallel directions and were observed to induce the interface deformation on the same order of magnitude. However, in our system, the interface deformation is in an orthogonal direction to the scattering force and is induced indirectly by the weakly coupled centrifugal effect.

In order to estimate the rate at which the experiments can be repeated, we calculate the characteristic time scales associated with the deformation and heat transfer of the system. For the dynamic response of the droplet with $a = 100\ \mu$m, the time for the interface to reach equilibrium is around $\tau = \mu a/\sigma \approx 4 \times 10^{-5}$ s. The time to reach the steady temperature is $\tau = L^2/\alpha \approx 3 \times 10^{-5}$ s, where $L \approx 1.5\ \mu$m is the size of the WGM mode volume and $\alpha \approx 8 \times 10^{-8}\ \mathrm{m}^2/\mathrm{s}$ is the thermal diffusivity of the resonator. Therefore, with different droplet radii assumed in our analysis, the response time of the system is estimated to be below 10^{-3} s.

B. Comparison of nonlinear effects

In this section, we compare the magnitude of nonlinear effects associated with the fundamental WGM $|l,l\rangle$, with the mode number l given by Table I. As discussed in Ref. [17,18], the droplet interface deformation may induce a WGM resonance frequency shift, which is similar to the Kerr effect. In addition, the increase of temperature in the droplet leads to the volume expansion as well as refractive index changes, which also result in WGM resonance frequency shifts. The refractive index change and the droplet radius expansion have been estimated in Ref. [18] as $\Delta n_T = (dn/dT)T_{\max}$ and $\Delta R_T = \alpha_T T_{\max}/3$, respectively, where $T_{\max}$ is the maximum temperature increase in the droplet, $dn/dT = -3.9 \times 10^{-4}\ \mathrm{K}^{-1}$ is the thermal coefficient of refractive index, and $\alpha_T = 8 \times 10^{-4}\ \mathrm{K}^{-1}$ is the thermal expansion coefficient of the proposed system.

Due to the Kerr effect, the refractive index of the liquid depends linearly on the optical field intensity. The maximum refractive index change can be estimated as $\Delta n \approx \chi^{(3)}|\boldsymbol{E}|^2_{\max}$, where $\chi^{(3)}$ is the third order nonlinear optical susceptibility and $|\boldsymbol{E}|_{\max}$ is the maximum electric field intensity in the droplet. We use the susceptibilities of water and carbon disulfide (CS_2) ($\chi^{(3)}_{\mathrm{water}} = 2.5 \times 10^{-22}\ \mathrm{m}^2/\mathrm{V}^2$ and $\chi^{(3)}_{\mathrm{CS}_2} = 3.1 \times 10^{-20}\ \mathrm{m}^2/\mathrm{V}^2$) to provide an order of magnitude estimate of the Kerr effect.

We now compare the magnitude of various nonlinear processes due to the radiation pressure, temperature induced droplet expansion and index change, thermocapillary force, Kerr effect and optical scattering force in liquid droplets. Let us define the interface deformation at the equator [$\Delta R(\theta = \pi/2)/a$] under radiation pressure, thermocapillary and light scattering effects as ΔR_{rad}, ΔR_{cap}, and $\Delta R_{\mathrm{scatt}}$, respectively. As shown in Fig. 7, interface deformation induced by the radiation pressure (ΔR_{rad}) is higher than other nonlinear effects. Additionally, nonlinearities associated with the

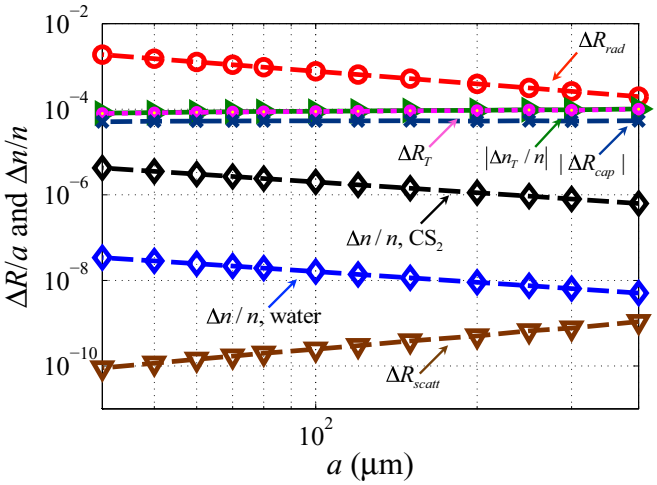

FIG. 7. Comparison of nonlinearities associated the radiation pressure, thermal effects, Kerr effect and light scattering. The $|\Delta R_{\rm cap}|$ and $\Delta R_{\rm scatt}$ curves are computed by the algorithm developed in Sec. II; all other curves are the same as shown in Fig. 6 of Ref. [18]. The power of the WGM in the droplet is assumed to be 1 W.

thermocapillarity, volume expansion and index change due to the temperature increase are also much stronger than the Kerr effect. The interface deformation induced by the light scattering, on the other hand, is smaller than the Kerr effect and thus should not play significant roles in droplets with diameter less than 1 mm. Finally, we point out that in order to support high-Q WGMs, the liquid that forms the microdroplet must possess low attenuation, which means that the value for ϖ should not exceed 100 m^{-1}. Therefore, for sub-mm-scale droplets that support high-Q WGMs, the nonlinearity induced by the scattering force can be safely ignored. Note that for large droplets with radii close to 1 mm, the interface deformation caused by the thermocapillary effect and the radiation pressure effect are of the same orders of magnitude and are in opposite directions. Therefore, liquid resonators with sizes on the scale of 100 μm or smaller should be used in the experiments in order to distinguish these two effects.

In addition to the optofluidic effects discussed in this work, the optical wave can also excite acoustic WGMs in resonators containing liquids [30,31]. Acoustic modes with frequencies up to 11 GHz and Q factors of the order of 10^3 were produced by forward and backward stimulated Brillouin scattering (SBS) in a microfluidic optomechanical resonator [31]. Such effect is also expected to exist in our system of liquid resonators. However, investigating SBS and acoustic WGMs in liquid resonators are beyond the scope of this work.

IV. CONCLUSION

In this paper, we develop boundary element models to calculate the fluid motion and droplet deformation due to the scattering force and thermocapillary force produced by a high-Q WGM in liquid droplets. The BIEs are derived in an axisymmetric domain that incorporate the effect of radiation pressure, scattering force and thermocapillary effect. We show that for droplets smaller than $a = 400$ μm, the radiation pressure should induce the highest velocity magnitude and the largest interface deformation, and thus lead to the strongest nonlinearity compared to the thermal effects, Kerr effect and light scattering. Due to the weakness of the centrifugal effect, the scattering force nonlinearity is several orders of magnitude smaller than the Kerr effect and thus can be safely neglected. The results presented here can guide future experimental studies of WGM-induced nonlinear optofluidic processes in liquid droplets.

ACKNOWLEDGMENT

This research was supported by the National Science Foundation (Grant No. CBET 1438112).

APPENDIX A: DERIVATION OF THE GREENS FUNCTIONS IN AXISYMMETRIC DOMAIN

We start by writing all the position, velocity, and force variables in Eq. (3) in terms of their x, r, and ϕ components. Without loss of generality, we assume $\boldsymbol{x}_0$ is located on the $\phi = 0$ plane, then the left-hand side of Eq. (3) can be expressed as $\boldsymbol{u}(\boldsymbol{x}_0) = (u_x, u_r, u_\phi)$. Similarly, variables on the right-hand side can be written as

$$\begin{aligned}
\boldsymbol{x} &= (x, r\cos\phi, r\sin\phi),\\
\boldsymbol{x}_0 &= (x_0, r_0, 0),\\
\boldsymbol{n} &= (n_x, n_r\cos\phi, n_r\sin\phi),\\
\boldsymbol{f} &= (f_x, f_r\cos\phi, f_r\sin\phi),\\
\boldsymbol{F} &= (0, -F_\phi\sin\phi, F_\phi\cos\phi),\\
\boldsymbol{u} &= (u_x, u_r\cos\phi, u_r\sin\phi) + (0, -u_\phi\sin\phi, u_\phi\cos\phi),\\
\boldsymbol{s} &= (x - x_0, r\cos\phi - r_0, r\sin\phi),\\
s &= |\boldsymbol{s}| = \left[(x - x_0)^2 + r^2 + r_0^2 - 2rr_0\cos\phi\right]^{1/2}. \qquad \text{(A1)}
\end{aligned}$$

Note that in Eq. (A1), all the velocity and force components $(u_x, u_r, u_\phi, f_x, f_r, F_\phi)$ are functions of (x, r) only. The only terms that are ϕ dependent are the Green's functions, which are predetermined. We can thus integrate the Green's functions in Eq. (3) along the ϕ direction analytically to reduce the dimension of numerical integration.

The single layer integral in Eq. (3) can be calculated as

$$\begin{aligned}
&\int_S G_{ji}(\boldsymbol{x}_0, \boldsymbol{x}) f_i(\boldsymbol{x})\, dS\\
&= \int_S (G_{jx} f_x + G_{jy} f_y + G_{jz} f_z)\, dS\\
&= \int_S [G_{jx} f_x + (G_{jy}\cos\phi + G_{jz}\sin\phi) f_r]\, dS\\
&= \int_C \begin{bmatrix} M_{xx} & M_{xr}\\ M_{rx} & M_{rr}\\ M_{\phi x} & M_{\phi r}\end{bmatrix} \begin{Bmatrix} f_x\\ f_r\end{Bmatrix} dl, \qquad \text{(A2)}
\end{aligned}$$

where

$$\begin{bmatrix} M_{xx} & M_{xr} \\ M_{rx} & M_{rr} \\ M_{\phi x} & M_{\phi r} \end{bmatrix}(\boldsymbol{x}_0,\boldsymbol{x}) = r\int_0^{2\pi} \begin{bmatrix} G_{xx} & G_{xy}\cos\phi + G_{xz}\sin\phi \\ G_{yx} & G_{yy}\cos\phi + G_{yz}\sin\phi \\ G_{zx} & G_{zy}\cos\phi + G_{zz}\sin\phi \end{bmatrix} d\phi. \quad \text{(A3)}$$

The integral of the Green's function over ϕ can be converted to elliptic integrals. For example,

$$M_{xx} = r\int_0^{2\pi} G_{xx}\,d\phi = r\int_0^{2\pi}\left(\frac{1}{s} + \frac{{d_x}^2}{s^3}\right)d\phi = r[I_{10} + d_x^2 I_{30}], \quad \text{(A4)}$$

where $d_x = x - x_0$, and [26]

$$I_{mn}(d_x,r,r_0) = c_m\int_0^{\pi/2} \frac{(2\cos^2\omega - 1)^n}{(1 - k^2\cos^2\omega)^{m/2}}d\omega, \quad \text{(A5)}$$

with

$$c_m = \frac{4k^m}{(4rr_0)^{m/2}}, \quad k^2 = \frac{4rr_0}{{d_x}^2 + (r + r_0)^2}. \quad \text{(A6)}$$

The integral in Eq. (A5) can be expressed by complete elliptic integrals of the first and second kind [$F(k)$ and $E(k)$, respectively] with the help of integral tables [32]. The values of $M_{\alpha\beta}$ for $\alpha,\beta = 1,2$ are the same as those derived in literature [26]. We can also show that $M_{\phi x} = M_{\phi r} = 0$.

The double layer integral in Eq. (3) can be calculated as

$$\begin{aligned}\int_S u_i(\boldsymbol{x})K_{ijm}(\boldsymbol{x},\boldsymbol{x}_0)n_m(\boldsymbol{x})\,dS(\boldsymbol{x}) &= \int_S \big[u_x K_{xjm}n_m + u_\sigma(K_{yjm}n_m\cos\phi + K_{zjm}n_m\sin\phi) \\ &\quad + u_\phi(-K_{yjm}n_m\sin\phi + K_{zjm}n_m\cos\phi)\big]\,dS \\ &= \int_C Q_{j\beta\gamma}u_\beta n_\gamma\,dl, \end{aligned} \quad \text{(A7)}$$

where in the last integral indices $j,\beta,\gamma = 1,2,3$, representing x,r,ϕ components. The value of $Q_{j\beta\gamma}$ in Eq. (A7) can be expressed as (note $n_\phi = 0$),

$$\begin{aligned} Q_{jxx} &= r\int_0^{\pi/2} K_{xjx}\,d\phi, \\ Q_{jxr} &= r\int_0^{\pi/2} (K_{xjy}\cos\phi + K_{xjz}\sin\phi)\,d\phi, \\ Q_{jrx} &= Q_{jxr} \\ Q_{jrr} &= r\int_0^{\pi/2} (K_{yjy}\cos^2\phi + 2K_{yjz}\sin\phi\cos\phi \\ &\quad + K_{zjz}\sin^2\phi)\,d\phi, \\ Q_{j\phi x} &= r\int_0^{\pi/2} (-K_{yjx}\sin\phi + K_{zjx}\cos\phi)\,d\phi, \\ Q_{j\phi r} &= r\int_0^{\pi/2} [-K_{yjy}\sin\phi\cos\phi \\ &\quad + K_{zjy}(\cos^2\phi - \sin^2\phi) + K_{zjz}\sin\phi\cos\phi]\,d\phi. \end{aligned} \quad \text{(A8)}$$

By substituting the Green's function Eq. (4) into Eq. (A8) and with the help of Eq. (A5), we can show that for $j,\beta,\gamma = 1,2$, the expressions of $Q_{j\beta\gamma}$ are the same as derived in literature. We can also show that for the new terms associated with the ϕ component ($j = 3$ or $\beta = 3$),

$$Q_{\phi x\gamma} = Q_{\phi r\gamma} = Q_{x\phi\gamma} = Q_{r\phi\gamma} = 0 \quad (\gamma = 1,2) \quad \text{(A9)}$$

and

$$\begin{aligned} Q_{\phi\phi x} &= 6r^2 r_0 d_x(I_{52} - I_{50}), \\ Q_{\phi\phi r} &= -6r^2 r_0[r_0(I_{53} - I_{51}) + r(I_{50} - I_{52})]. \end{aligned} \quad \text{(A10)}$$

Similarly, the volume integral in Eq. (3) can be simplified as

$$\begin{aligned}\int_V G_{ji}(\boldsymbol{x}_0,\boldsymbol{x})F_i(\boldsymbol{x})\,dV(\boldsymbol{x}) &= \int_A \left[r\int_0^{2\pi} G_{ji}(\boldsymbol{x}_0,\boldsymbol{x})F_i(\boldsymbol{x})\,d\phi\right]dA(\boldsymbol{x}) \\ &= \int_A r M_{j\phi}(\boldsymbol{x}_0,\boldsymbol{x})F_\phi\,dA(\boldsymbol{x}), \end{aligned} \quad \text{(A11)}$$

where we have defined

$$M_{j\phi}(\boldsymbol{x}_0,\boldsymbol{x}) = r\int_0^{2\pi} [-G_{j2}(\boldsymbol{x}_0,\boldsymbol{x})\sin\phi + G_{j3}(\boldsymbol{x}_0,\boldsymbol{x})\cos\phi]\,d\phi. \quad \text{(A12)}$$

It is easy to show that

$$M_{x\phi} = M_{r\phi} = 0, \quad \text{(A13)}$$

and

$$\begin{aligned} M_{\phi\phi}(\boldsymbol{x}_0,\boldsymbol{x}) &= r\int_0^{2\pi} [-G_{32}(\boldsymbol{x}_0,\boldsymbol{x})\sin\phi + G_{33}(\boldsymbol{x}_0,\boldsymbol{x})\cos\phi]\,d\phi \\ &= r\int_0^{2\pi}\left[-\frac{r(r\cos\phi - r_0)}{s^3}\sin^2\phi + \left(\frac{1}{s} + \frac{r^2\sin^2\phi}{s^3}\right)\cos\phi\right]d\phi \\ &= r[I_{11} + rr_0(I_{30} - I_{32})]. \end{aligned} \quad \text{(A14)}$$

It is obvious now that Eqs. (A2), (A7), and (A11) lead to Eq. (5), and all the Green's functions in the axisymmetric domain are explicitly determined in this section.

APPENDIX B: SINGULARITY OF GREEN'S FUNCTIONS

Let us define the distance between $\boldsymbol{x}$ and $\boldsymbol{x}_0$ on a ϕ = constant plane as $\boldsymbol{d} = (d_x,d_r) = (x - x_0, r - r_0)$ and $d = [(x - x_0)^2 + (r - r_0)^2]^{1/2}$. It has been shown in literature [26,33] that as $\boldsymbol{x} \to \boldsymbol{x}_0$, $M_{xx}, M_{rr} \to -2\ln(d)$, while M_{xr}, M_{rx}, and $Q_{\alpha\beta\gamma}n_\gamma$ are finitely bounded, for $\alpha,\beta,\gamma = 1,2$. We now show that the newly derived nontrivial terms in this work, $M_{\phi\phi}$ and $Q_{\phi\phi\gamma}n_\gamma$, also exhibit $\mathcal{O}(\ln(d))$ type singularity.

From Eq. (A5) and with the help of [32], we can show that

$$\begin{aligned} I_{11} &= \frac{c_1}{k^2}[-2E - (k^2 - 2)F], \\ I_{30} - I_{32} &= \frac{4c_3}{k^4}[-2E - (k^2 - 2)F], \end{aligned} \quad \text{(B1)}$$

where F and E are complete elliptic integrals of the first and second kind, whose definition and asymptotic behaviors are

$$F(k) = \int_0^{\pi/2} \frac{1}{(1-k^2\cos^2\xi)}\, d\xi \to -\ln(d),$$
$$E(k) = \int_0^{\pi/2} (1-k^2\cos^2\xi)\, d\xi \to 1. \tag{B2}$$

Therefore, Eq. (A14) leads to

$$M_{\phi\phi} = -\frac{4}{k}\sqrt{\frac{r}{r_0}}[2E + (k^2-2)F] \to -4\ln(d). \tag{B3}$$

Similarly, we can show

$$I_{52}-I_{50} = c_5\left[\frac{8}{3k^4}F + \frac{4(k^2-2)}{3k^4k'}E\right],$$
$$I_{53}-I_{51} = \frac{4c_5}{3k^6k'^2}[-8k'^2(k^2-2)F - (k^4-16k^2+16)E], \tag{B4}$$

with $k'^2 = 1-k^2$. The values of $Q_{\phi\phi\gamma}(\gamma = 1,2)$ exhibit strong singularities ($\sim 1/d^2$). However, the product of $Q_{\phi\phi\gamma}$ and n_γ, i.e., $q_{33} = Q_{\phi\phi\gamma}n_\gamma$, may exhibit weaker singularity. Here we compute q_{33} explicitly,

$$\begin{aligned} q_{33} &= Q_{\phi\phi x}n_x + Q_{\phi\phi r}n_r \\ &= 6r^2r_0[(d_xn_x + rn_y)(I_{52}-I_{50}) + r_0n_y(I_{51}-I_{53})] \\ &= \frac{8r^2r_0c_5}{k^6}[g_F(k)F + g_E(k)E], \end{aligned} \tag{B5}$$

where g_F and g_E are functions k, which can be simplified as

$$\begin{aligned} g_F(k) &= 2[(d_xn_x + rn_y + 4r_0n_y)k^2 - 8r_0n_y] \\ &\to 2(dn_x - 3r_0)n_y \quad (\boldsymbol{x} \to \boldsymbol{x}_0), \\ g_E(k) &= \frac{1}{k'^2}[(d_xn_x + rn_y + r_0n_y)k^4 \\ &\quad - (d_xn_x + rn_y + r_0n_y)k^2 + 16r_0n_y] \\ &= \frac{1}{k'^2}[-(d_xn_x + d_rn_y)k^2 + 16r_0n_yk'^2 - 2r_0n_yk^2k'^2]. \end{aligned} \tag{B6}$$

Note that in the last equation of Eq. (B6), $\boldsymbol{d}$ becomes orthogonal to $\boldsymbol{n}$ as $\boldsymbol{x} \to \boldsymbol{x}_0$, and $\boldsymbol{d}\cdot\boldsymbol{n} \sim d^2$. Therefore g_E is non-singular. Combining Eqs. (B2), (B5), and (B6) and noting $d\ln(d) \to 0$ as $d \to 0$, we have

$$q_{33} \to \frac{8r_0^3c_5}{k^6}[6r_0n_y\ln(d)] \to \frac{6n_y}{r_0}\ln(d). \tag{B7}$$

In the present work $\boldsymbol{x}$ and $\boldsymbol{x_0}$ are located on a circle with unit radius; in this case we have $q_{33} \to 6\ln(d)$.

The presence of $\psi\ln(d)$ ($\psi = -2, -4$ or 6) singularities may cause large numerical integration error. To reduce the numerical error, the singularity can be subtracted from the singular Green's functions to make the integration nonsingular. The analytic integral of $\psi\ln(d)$ should then be added back to the nonsingular integral. This technique has also been used in literature and proved to be highly accurate [25–27,33].

[1] Z. Li and D. Psaltis, Optofluidic dye lasers, Microfluid Nanofluidics **4**, 145 (2007).

[2] F. Vollmer, D. Braun, A. Libchaber, M. Khoshsima, I. Teraoka, and S. Arnold, Protein detection by optical shift of a resonant microcavity, Appl. Phys. Lett. **80** 4057 (2002).

[3] H. Zhu, I. M. White, J. D. Suter, P. S. Dale, and X. Fan, Analysis of biomolecule detection with optofluidic ring resonator sensors, Opt. Express **15**, 9139 (2007).

[4] A. Casner and J.-P. Delville, Adaptative lensing driven by the radiation pressure of a continuous-wave laser wave upon a near-critical liquid–liquid interface, Opt. Lett. **26**, 1418 (2001).

[5] A. Werber and H. Zappe, Tunable microfluidic microlenses, Appl. Opt. **44**, 3238 (2005).

[6] U. Levy and R. Shamai, Tunable optofluidic devices, Microfluid Nanofluidics **4**, 97 (2008).

[7] A. Ashkin and J. M. Dziedzic, Radiation Pressure on a Free Liquid Surface, Phys. Rev. Lett. **30**, 139 (1973).

[8] I. Komissarovak, G. Ostrovskaya, and E. Shedova, Light pressure induced deformations of a free liquid surface, Opt. Commun. **66**, 15 (1988).

[9] H. M. Lai, P. T. Leung, K. L. Poon, and K. Young, Electrostrictive distortion of a micrometer-sized droplet by a laser pulse, J. Opt. Soc. Am. B **6** 2430 (1989).

[10] I. Brevik and R. Kluge, Oscillations of a water droplet illuminated by a linearly polarized laser pulse, J. Opt. Soc. Am. B **16**, 976 (1999).

[11] A. Casner, J.-P. Delville, and I. Brevik, Asymmetric optical radiation pressure effects on liquid interfaces under intense illumination, J. Opt. Soc. Am. B **20** 2355 (2003).

[12] E. Brasselet, R. Wunenburger, and J.-P. Delville, Liquid Optical Fibers with a Multistable Core Actuated by Light Radiation Pressure, Phys. Rev. Lett. **101**, 014501 (2008).

[13] J.-P. Delville, M. Robert de Saint Vincent, R. D. Schroll, H. Chraïbi, B. Issenmann, R. Wunenburger, D. Lasseux, W. W. Zhang, and E. Brasselet, Laser microfluidics: Fluid actuation by light, J. Opt. A: Pure Appl. Opt. **11**, 034015 (2009).

[14] H. Chraibi, R. Wunenburger, D. Lasseux, J. Petit, and J.-P. Delville, Eddies and interface deformations induced by optical streaming, J. Fluid Mech. **688**, 195 (2011).

[15] S. A. Ellingsen, Microdroplet oscillations during optical pulling, Phys. Fluids **24**, 022002 (2012).

[16] S. Å. Ellingsen, Theory of microdroplet and microbubble deformation by Gaussian laser beam, J. Opt. Soc. Am. B **30**, 1694 (2013).

[17] Y. Xu, P. Zhang, S. Jung, and A. Lee, Analysis of radiation pressure induced nonlinear optofluidics, Opt. Express **22**, 28875 (2014).

[18] P. Zhang, S. Jung, A. Lee, and Y. Xu, Radiation-pressure-induced nonlinearity in microdroplets, Phys. Rev. E **92**, 063033 (2015).

[19] C. N. Baroud, J.-P. Delville, F. Gallaire, and R. Wunenburger, Thermocapillary valve for droplet production and sorting, Phys. Rev. E **75**, 046302 (2007).

[20] R. Wunenburger, B. Issenmann, E. Brasselet, C. Loussert, V. Hourtane, and J. P. Delville, Fluid flows driven by light scattering, J. Fluid Mech. **666**, 273 (2010).

[21] R. Schroll, R. Wunenburger, A. Casner, W. Zhang, and J.-P. Delville, Liquid Transport due to Light Scattering, Phys. Rev. Lett. **98**, 133601 (2007).

[22] C. N. Baroud, M. Robert de Saint Vincent, and J.-P. Delville, An optical toolbox for total control of droplet microfluidics, Lab Chip **7**, 1029 (2007).

[23] M. Robert de Saint Vincent, R. Wunenburger, and J.-P. Delville, Laser switching and sorting for high speed digital microfluidics, Appl. Phys. Lett. **92**, 154105 (2008).

[24] J. D. Jackson, *Classical Electrodynamics*, 3rd ed. (John Wiley & Sons, New York, 1998).

[25] S. Lee and L. Leal, The motion of a sphere in the presence of a deformable interface: II. A numerical study of the translation of a sphere normal to an interface, J. Colloid Interface Sci. **87**, 81 (1982).

[26] C. Pozrikidis, *Boundary Integral and Singularity Methods for Linearized Viscous Flow* (Cambridge University Press, Cambridge, 1992).

[27] R. H. Davis, Buoyancy-driven viscous interaction of a rising drop with a smaller trailing drop, Phys. Fluids **11**, 1016 (1999).

[28] A. Prosperetti and G. Tryggvason, *Computational Methods for Multiphase Flow* (Cambridge University Press, Cambridge, 2007).

[29] S. R. Palit, Thermodynamic interpretation of the Eötvös constant, Nature (London) **177**, 1180 (1956).

[30] G. Bahl, M. Tomes, F. Marquardt, and T. Carmon, Observation of spontaneous brillouin cooling, Nat. Phys. **8**, 203 (2012).

[31] G. Bahl, K. H. Kim, W. Lee, J. Liu, X. Fan, and T. Carmon, Brillouin cavity optomechanics with microfluidic devices, Nat. Commun. **4** 1994 (2013).

[32] I. S. Gradshteyn and I. M. Ryzhik, in *Table of Integrals, Series, and Products*, 8th ed., edited by D. Zwillinger and V. Moll (Academic Press, Boston, 2014), pp. 184–196.

[33] W. Hackbusch, *Integral Equations: Theory and Numerical Treatment* (Birkhauser, Basel, 1995).